



The importance of Canadian Arctic Archipelago gateways for glacial expansion in Scandinavia

Marcus Lofverstrom¹ , Diane M. Thompson¹, Bette L. Otto-Bliesner²  and Esther C. Brady²

The last glacial cycle began around 116,000 years before present during a period with low incoming solar radiation in Northern Hemisphere summer. Following the glacial inception in North America, the marine sediment record depicts a weakening of the high-latitude ocean overturning circulation and a multi-millennial eastward progression of glaciation across the North Atlantic basin. Modelling studies have shown that reduced solar radiation can initiate inception in North America and Siberia; however, the proximity to the temperate North Atlantic typically precludes ice growth in Scandinavia. Using a coupled Earth-system-ice-sheet model, we show that ice forming in North America may help facilitate glacial expansion in Scandinavia. As large coherent ice masses form and start filling the ocean gateways in the Canadian Archipelago, the transport of comparatively fresh North Pacific and Arctic water through the archipelago is diverted east of Greenland, resulting in a freshening of North Atlantic deep convection regions, sea-ice expansion and a substantial cooling that is sufficient to trigger glacial inception in Scandinavia. This mechanism may also help explain the Younger Dryas cold reversal and the rapid regrowth of the Scandinavian Ice Sheet following several warm events in the last glacial period.

Substantial research efforts have been devoted to understanding the causes of Earth's glacial–interglacial cycles. The orbital theory proposed by ref. ¹, which links ice nucleation and growth to periods with low summer insolation (incoming solar radiation at the top of the atmosphere), is perhaps the most robust first-order explanation of glacial cycles to date. The fidelity of the orbital theory is supported by the most recent glacial inception, which coincided with a Northern Hemisphere summer insolation minimum (centred on 116,000 years before present (116 ka); see Fig. 1a and Extended Data Fig. 1)¹, despite the fact that atmospheric greenhouse gas concentrations, the land–ocean configuration and eustatic sea level were close to CE 1850 pre-industrial values^{2,3}. Numerous globally distributed, proxy-data archives indicate that the initial ice-sheet growth was both rapid and substantial and lowered the global sea level by as much as 30–50 m between approximately 120 and 110 ka^{2–5}. Ice-rafted debris (IRD, material deposited on the ocean floor by icebergs) in the North Atlantic also increased during this period^{6–11} (Fig. 1), suggesting that many of the early ice sheets were both marine terminating and dynamically active.

Tangible geological and geomorphological evidence of the incipient ice sheets remains elusive; however, it is generally thought that the early ice-sheet growth occurred in the southern Canadian Arctic Archipelago (CAA), around Hudson Bay, on Spitsbergen and other islands in the Arctic Ocean, along the Barents and Kara seaboards in west-central Siberia and in the highland regions of Scandinavia and western North America^{12–17} (Fig. 2). While there is evidence of early (although possibly smaller scale and/or ephemeral^{14,18}) ice growth in the broader CAA region—including ice-sheet flow patterns^{14,15} and IRDs with CAA provenance in both the Arctic Ocean and Baffin Bay^{11,18,19}—there is currently no evidence-based geological reconstruction of a proto-Innuitian Ice Sheet. There is, however, reliable evidence of spatially extensive but comparatively short-lived ice caps in northeastern Siberia and in the interior of Alaska^{20,21}, where atmospheric circulation changes^{21–25} induced by the Laurentide–Cordilleran ice-sheet complex precluded large coherent ice masses

in the latter stages of the last glacial period^{12,20,21}. Even though all of the aforementioned inception regions support varying levels of glaciation today, the climate in Scandinavia is considerably more temperate than in the other locations because of heat transport by predominantly southwesterly winds across the North Atlantic and due to its proximity to the comparatively warm and perennially ice-free Nordic Seas^{26,27}.

Evidence from proxy data

While the general inception regions are known, the exact timing and location of ice nucleation in the last glacial period are debated. The challenge is due primarily to a paucity of reliably dated terrestrial land forms and proxy data from this period, as evidence of early glaciation has been obliterated by overriding ice sheets at later stages of the glacial period^{12,13,17,28}. The most abundant proxy records are therefore marine, consisting primarily of IRDs and the geochemical signature and relative abundance of various species of planktic and benthic foraminifera⁶ in ocean sediments. These marine sediment cores provide evidence of a time-delayed inception in Scandinavia (by as much as 2,000–5,000 years), dictated by the equatorward migration of Arctic water and a weakened Atlantic meridional overturning circulation (AMOC) in high latitudes.

First, proxy records show a decline in sea surface temperature (SST, red line in Fig. 1b,d) and a rise in the proportion of cold-water foraminifera (left/sinistral coiling *Neogloboquadrina pachyderma*²⁹; blue line in Fig. 1b) with the decline in Northern Hemisphere summer insolation between 125 and 118 ka. More negative *N. pachyderma* stable carbon isotope ($\delta^{13}\text{C}$) values during this interval indicate strong Atlantic water influence within the Norwegian Sea and Fram Strait (green line in Fig. 1c,d), suggesting a strong AMOC and comparatively warm conditions in the northeastern North Atlantic^{6–9} (thus precluding ice formation in Scandinavia).

The first major IRD events occur by 118 ka in the western North Atlantic (interval 'I' in Fig. 1b), consistent with a substantial growth of an incipient North American Ice Sheet. By contrast, IRDs are delayed

¹Department of Geosciences, University of Arizona, Tucson, AZ, USA. ²Climate and Global Dynamics Laboratory, National Center for Atmospheric Research, Boulder, CO, USA. ✉e-mail: lofverstrom@arizona.edu

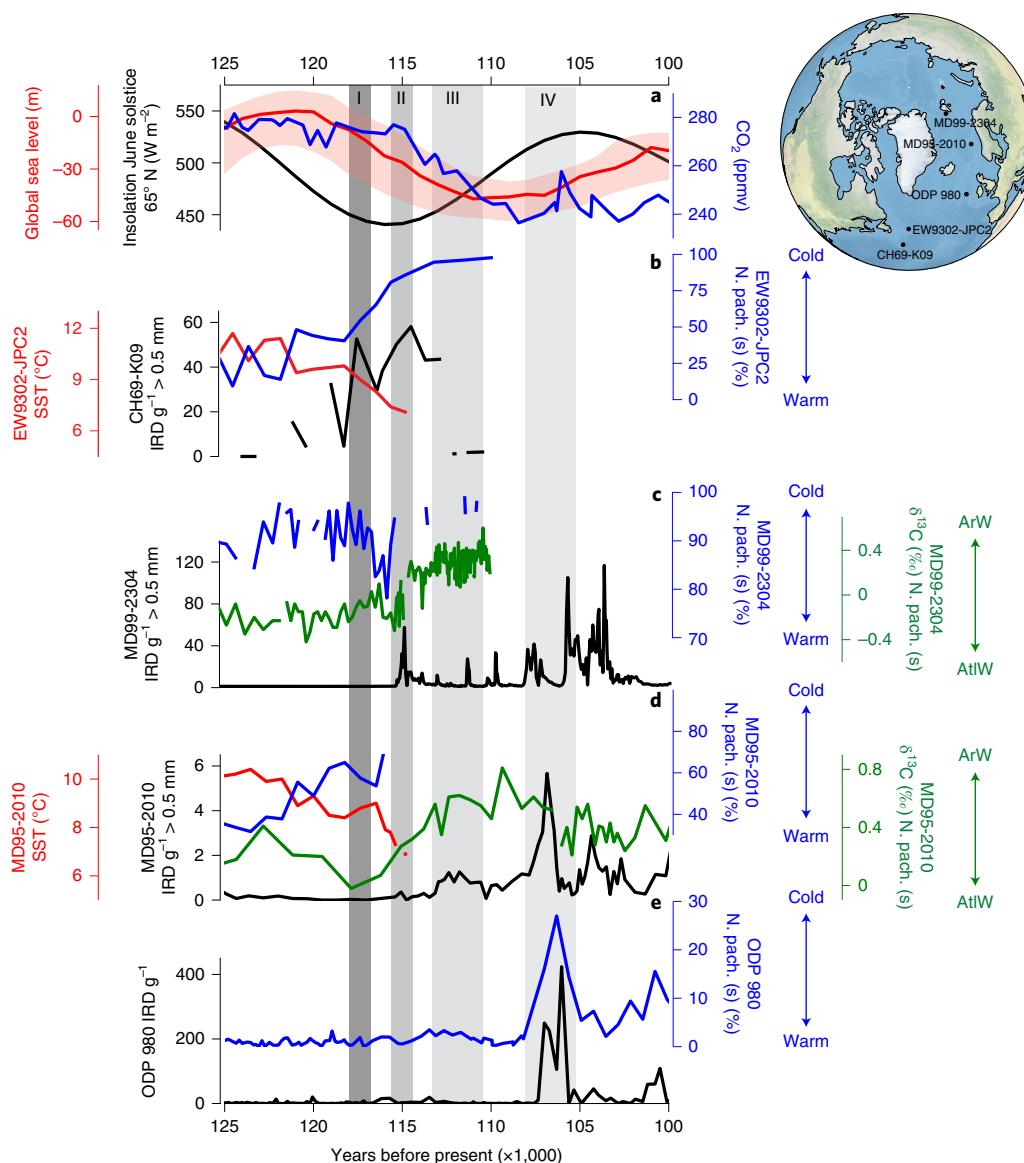


Fig. 1 | Time series of proxy data across the inception interval. **a**, Global sea-level change³, top-of-atmosphere insolation at 65°N at June solstice¹ and CO₂ concentration⁵¹. **b–e**, Data from North Atlantic sediment cores. Coloured lines in **b–e** depict SST (red), IRD (black), abundance of *Neogloboquadrina pachyderma sinistral* (N. pach. (s); blue), a planktonic foraminifera indicator species for polar waters and its $\delta^{13}\text{C}$ variations ($\delta^{13}\text{C}$ N. pach. (s); green). Positive/negative $\delta^{13}\text{C}$ N. pach. (s) indicates dominance of Arctic water (ArW)/Atlantic water (AtIW), respectively. Panels depict data from the western (cores CH69-K09 and EW9302-JPC2; ref. ⁶) (**b**), northeastern (core MD99-2304; refs. ^{6–8}) (**c**), eastern (core MD95-2010; refs. ^{7b}) (**d**) and east-central (core ODP 980; refs. ^{6,10}) (**e**) North Atlantic, respectively. Proxy-data sites are indicated in the top right corner. Discontinuous lines in **b–d** are due to missing data in the proxy datasets. Maps generated using Cartopy with Natural Earth shapefiles.

until well into the inception period in the eastern North Atlantic. Proxy data suggest that this delay in ice development and IRDs may be attributed to a strong AMOC between 118.0 and 115.5 ka, as evidenced by the abrupt decline in $\delta^{13}\text{C}$ and decreases in cold-water foraminifera, with the northern site lagging behind the southern site (Fig. 1c,d)^{6,10}.

An abrupt reversal of this pattern occurs after the insolation minima at 115.5–114.0 ka ('II' in Fig. 1), with more positive $\delta^{13}\text{C}$ and an increased abundance in cold-water species, changes that are coincident with an IRD pulse at the northernmost site in the Fram Strait (Spitsbergen, Fig. 1c). Together, this suggests a weakening of the northern branch of the AMOC, increased Arctic influence in the Nordic Seas and ice growth at the northernmost margins of the incipient Scandinavian Ice Sheet^{6–9}. The gradual increase in $\delta^{13}\text{C}$

and Arctic water influence in the eastern North Atlantic continues from 114 to 108 ka, with IRD pulses beginning further south off mainland Scandinavia by 113 ka ('III' in Fig. 1d) and off the British Isles by 108–105 ka ('IV' in Fig. 1d), consistent with ice growing at more southern locations^{6–8,30}.

Importance of Arctic freshwater transport

Temperature and salinity transport into the northern North Atlantic are instrumental for regulating density-driven deep convection (and other mixing processes) in the Labrador, Irminger and Nordic seas (Fig. 2), the main deep-water formation regions of the overturning circulation^{31,32}. At high latitudes, ocean density is more strongly influenced by salinity than by temperature³³. Consequently, a comparatively small reduction in salinity from freshwater input

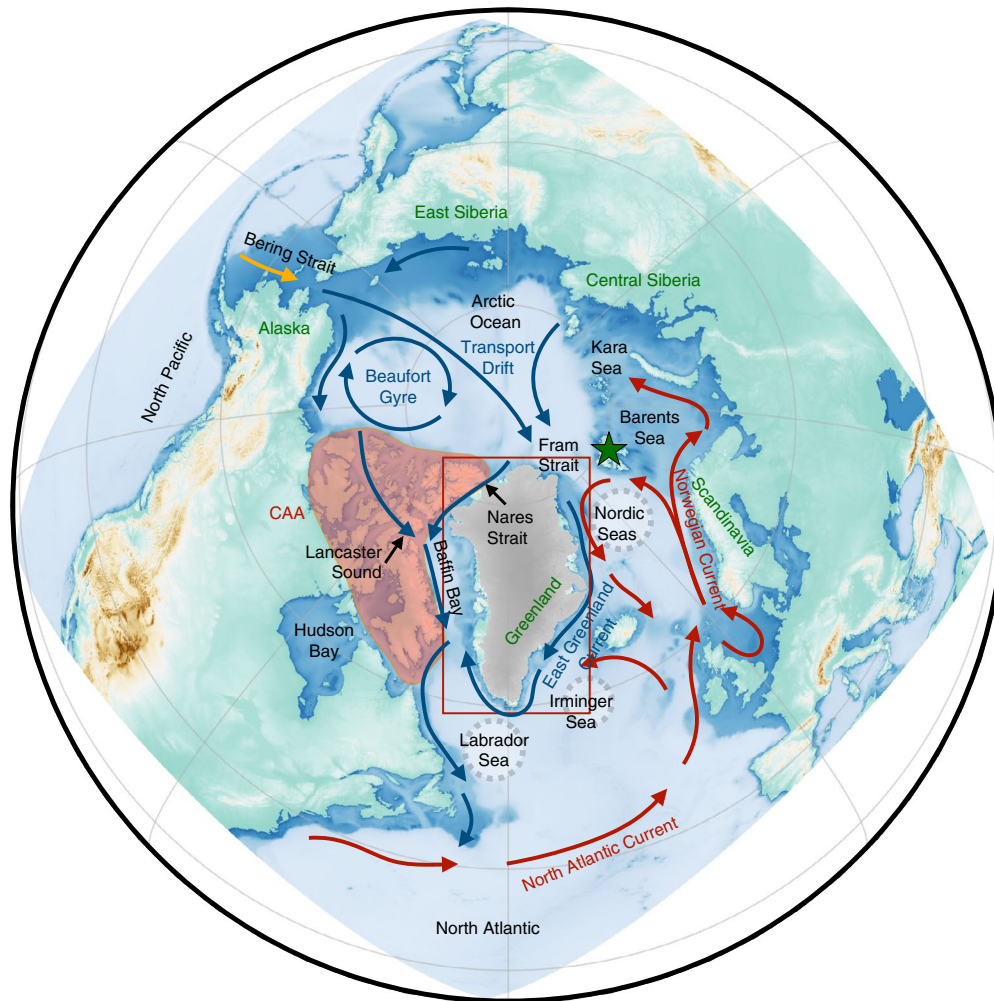


Fig. 2 | Map of regions and major currents in the Northern Hemisphere high latitudes. Ocean regions and primary Arctic ocean gateways are denoted by black text, and land regions are denoted by green text; Spitsbergen is indicated by a green star, and the CAA is highlighted by orange shading. Arrows show ocean currents with Pacific (orange), Atlantic (red) and Arctic (blue) provenance. Dashed circles in the Labrador Sea, the Irmingier Sea and the Nordic Seas indicate the approximate locations of North Atlantic deep convection regions that drive the meridional overturning circulation. The background map is showing topography and bathymetry as represented on the 4×4 km ice-sheet model grid (Methods). This grid has $2,592 \times 2,592$ grid cells and matches the resolution of the default ice-sheet model grid currently supported by CESM2 (outlined by the red box around Greenland).

can weaken convective overturning, even in the case of surface cooling³⁴; by contrast, an increase in high-latitude salinity can have the opposite effect and strengthen convective overturning.

However, as previous studies have shown^{35–37}, both the AMOC strength and the North Atlantic climate are potentially sensitive to the status of the ocean gateways in the Arctic. At present, the North Pacific is less saline and has a relatively higher sea surface height than the Arctic Ocean. The flow across Bering Strait is therefore largely one directional and constitutes a net freshwater transport into the Arctic basin and subsequently into the North Atlantic³⁸. Additional freshwater input into the Arctic basin comes from river transport and seasonal snow and sea-ice melt. This relatively fresh water from the Arctic enters the North Atlantic via two primary routes (Fig. 2): (1) through Fram Strait east of Greenland³⁴ and (2) through the CAA into the Labrador Sea (primarily via Nares Strait³⁹ and Lancaster Sound⁴⁰). The net freshwater flux through Lancaster Sound (about 75 ± 10 mSv (ref. ³⁹)) is approximately twice as large as the net

freshwater flux through Nares Strait (about 34 ± 6 mSv (ref. ³⁹)) and is thus likely to be more important for regulating the northwestern North Atlantic salinity budget and convective overturning.

Moreover, observational surveys of currents and salinity in Lancaster Sound and Nares Strait reveal a strongly stratified flow with the freshest water near the surface (around 30–31 PSU in the upper tens of metres of the water column) and more saline water at depth (around 35 PSU, which is similar to the North Atlantic)^{39,40}. Due to the strong salinity stratification, the formation of a thick floating ice shelf in the CAA (let alone a grounded marine ice sheet) would probably be sufficient to inhibit the freshwater flux through the archipelago and into the northwestern North Atlantic.

Simulating glacial inception

We use a coupled Earth-system–ice-sheet model—the Community Earth System Model, version 2 (CESM2)⁴¹ with a 4 km ice-sheet model grid covering a large fraction of the Northern Hemisphere

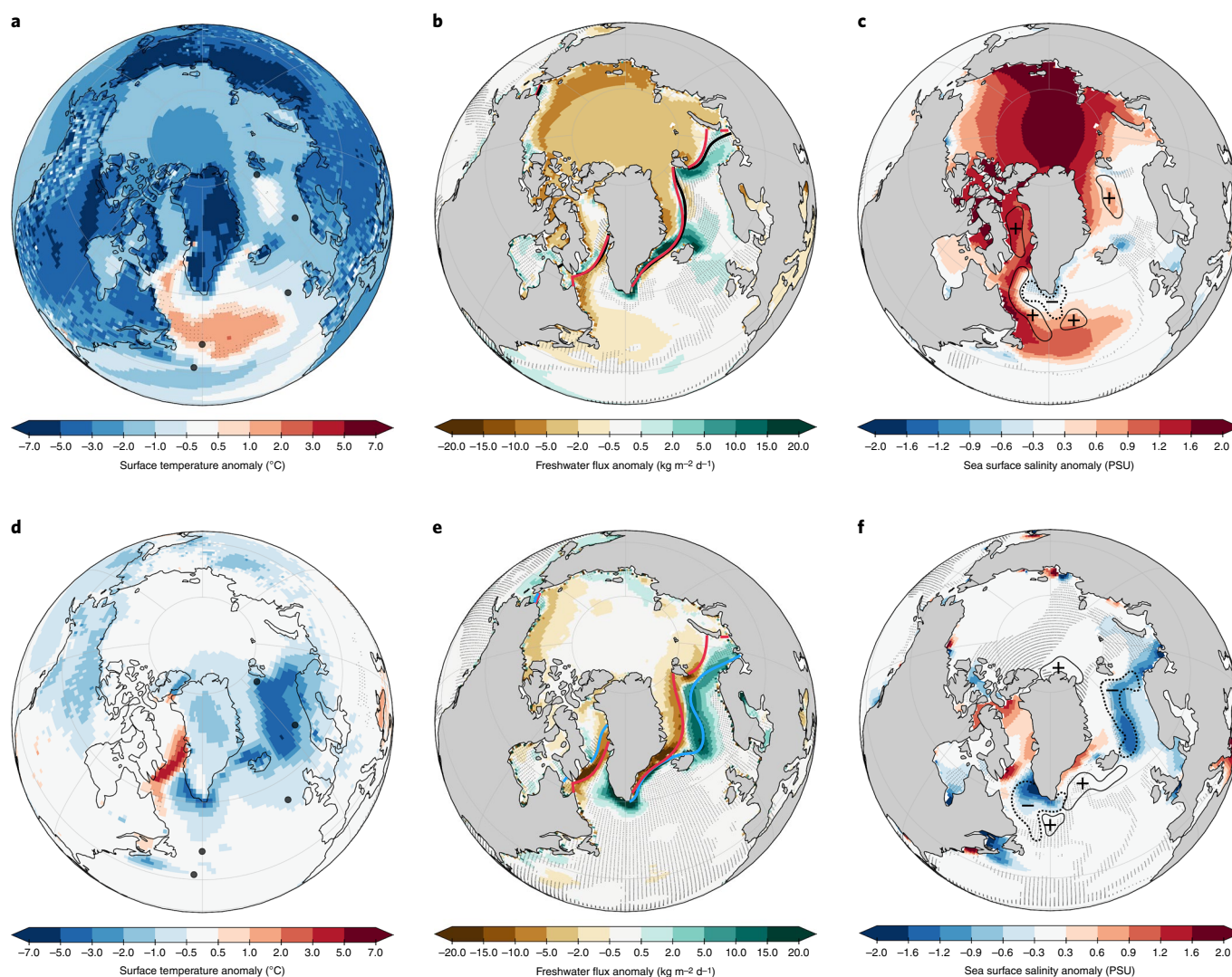


Fig. 3 | Climate response to 116 ka insolation and greenhouse gas forcing and to the closing of the CAA ocean gateways. **a–c**, The difference between the 116 ka simulation with open CAA gateways and the pre-industrial control simulation for boreal summer (June–July–August (JJA)) surface temperature anomaly (filled circles indicate proxy-data sites in Fig. 1) (**a**), JJA freshwater flux anomaly (shading) and 50% sea-ice margin in the pre-industrial (black contours) and the 116 ka simulation with open CAA gateways (red contours), respectively (**b**) and JJA sea surface salinity anomaly (shading) and annual mean mixed-layer depth anomaly in contours (solid/dashed lines denote positive/negative mixed-layer depth anomalies, respectively) (**c**). **d–f**, The corresponding response to closed CAA gateways with respect to the 116 ka simulation with open CAA gateways; contours in **e** indicate the 50% JJA sea-ice margin in the 116 ka simulation with open (red contours) and closed (blue contours) CAA ocean gateways, respectively. Stippling indicates differences that are not significant at the 95% level. Maps generated using Cartopy with Natural Earth shapefiles.

(Fig. 2; Methods)—to demonstrate that the formation of a marine ice shelf in the CAA could have played an important role in glacial inception over Scandinavia. Two simulations of the 116 ka period are carried out: one where the CAA gateways remain open and one otherwise identically forced simulation where the CAA gateways are closed (Extended Data Fig. 2). The latter is emulating the cessation of a water exchange between the Arctic and the western North Atlantic by the presence of a marine ice shelf in the CAA region.

Similar to previous modelling studies^{42–45}, we find that cool summer surface temperatures induced by the 116 ka orbital configuration are sufficient to initiate ice-sheet growth in the CAA: on the islands in the Barents and Kara seas and along the Siberian Arctic coast (compare Figs. 3a and 4a; see also Extended Data Fig. 3). Distinct ice masses also form in northeastern Siberia and in the highland regions of Alaska, broadly consistent with proxy-data evidence^{20,21}. Conversely, even though the summer climate in Scandinavia is cooler than in the pre-industrial simulation, this

region remains sufficiently mild to prevent the formation of a thick perennial snow cover, which is a prerequisite for ice growth.

Despite the reduced summer insolation, temperate sea surface conditions are maintained in the central and northeastern North Atlantic (Fig. 3a) due to increased poleward heat transport from an invigorated AMOC (Extended Data Fig. 4). The strong AMOC is primarily a response to a more saline Arctic basin owing to reduced Arctic sea-ice melt (compare Fig. 3b and Extended Data Fig. 5), although the summer sea-ice edge is broadly similar to that of the pre-industrial simulation. Deep convection is therefore not only maintained but invigorated in both the Labrador and Nordic Seas (annual mean mixed-layer depth is used as a heuristic of deep-water formation in Fig. 3c). This result is consistent with proxy-data evidence for a strong AMOC that counteracted orbital cooling before the 116 ka insolation minimum^{6–10,30,46} (Fig. 1). Moreover, these results are broadly consistent with ref. 45, who showed that the summer surface temperatures in Scandinavia are

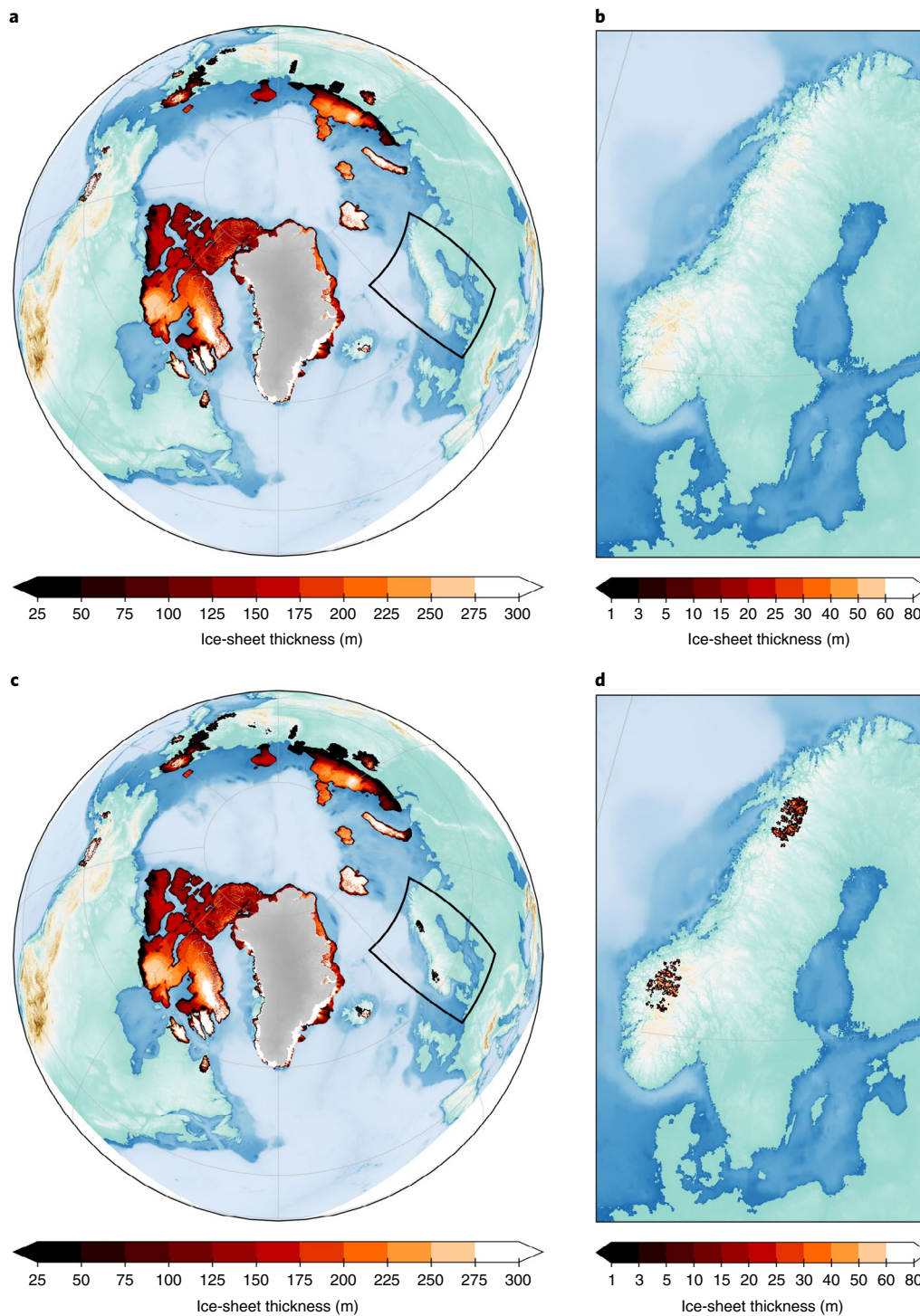


Fig. 4 | Simulated ice-sheet thickness in the simulation with open and closed ocean gateways in the CAA, respectively. **a**, Simulated ice-sheet thickness in the 116 ka simulation with open CAA ocean gateways. **b**, More-detailed view of Scandinavia (region indicated by black box in **a**). Note that there is no ice growth in Scandinavia in this simulation. **c**, Simulated ice-sheet thickness in the 116 ka simulation with closed CAA ocean gateways. **d**, More-detailed view of Scandinavia (region indicated by black box in **c**). The Greenland Ice Sheet is fully interactive in these simulations; however, the initial Greenland extent is indicated by grey shading for plotting purposes. The background map is showing topography and bathymetry as represented on the 4 × 4 km ice-sheet model grid.

3–4°C too warm for inception to occur under the 116 ka summer insolation minimum. They further posited that a weaker AMOC and a reduced poleward ocean heat transport, paired with an increased equatorward migration of sea ice in the Nordic Seas, could potentially induce a sufficiently strong regional cooling to

trigger inception in Scandinavia. However, this hypothesis was based on a sensitivity simulation with a prescribed, artificially induced surface cooling in the northeastern North Atlantic, and no modelling experiment to date has demonstrated a mechanism that can induce this climate response.

The simulated ice sheet covering the CAA region in Fig. 4a is 100–200 m thick, including the marine ice among the islands. Although this is not sufficient to fully close the ocean gateways (sill depths are typically 150–200 m (refs. 39,40)) and thus completely switch off the regional Arctic–North Atlantic water exchange, it is probably sufficiently thick to strongly disrupt the highly stratified freshwater transport^{39,40} through the archipelago. We note that realistic representation of ocean interactions with marine ice sheets is an active area of development in CESM, and it is currently not possible to simulate a gradual closing of ocean gateways by floating ice shelves. Investigating the impact of partial gateway closures by ice shelves, including experiments where different gateways are closed in isolation (notably, Nares Strait and Lancaster Sound) is therefore left to future work. Furthermore, we note that the simulated ice cover (Fig. 4) in the northern and western CAA is a bit too extensive compared with proxy evidence of early ice growth in this region^{11,14,15,18,19}; for example, the recent ice-sheet reconstruction by ref. 17 depicts a comparatively smaller ice cap confined to the southern CAA. Nevertheless, the reconstruction in ref. 17 also suggests glacial obstruction of the key ocean gateways that we explore in the sensitivity simulation described below.

The simulated climate response to a closing of the CAA gateways (under the 116 ka forcing protocol; Methods) is presented in Fig. 3d–f. Most prominently, there is a strong regional freshening and cooling of the Nordic Seas and a cooling of Scandinavia, and two spatially separated ice caps form in the Scandinavian mountain range (Fig. 4c,d). When the CAA gateways are closed, the comparatively fresh water that normally would enter the western North Atlantic through the archipelago is instead transported around the eastern side of Greenland (primarily through Fram Strait), where it affects the sensitive deep convection regions in the Nordic Seas and in the Labrador Sea (via the East Greenland Current; compare Figs. 2 and 3d–f). As a result, the high-latitude branch of the overturning circulation is substantially weakened (Extended Data Fig. 4), resulting in cooling and an equatorward migration of the sea-ice margin in the Nordic Seas (Fig. 3d,e). Freshwater input from seasonal sea-ice melting acts as a positive feedback that helps maintain the diminished convection and overturning circulation (compare Fig. 3 and Extended Data Fig. 6).

The cool sea surface conditions in the Nordic Seas are in turn advected over Scandinavia by the mean winds over the North Atlantic (Extended Data Fig. 7); the Scandinavian summer climate is therefore several degrees cooler than in the simulation with open CAA gateways, with local cooling of 4–6 °C in the mountains where perennial snow and ice are established (Fig. 3d; the high-elevation temperature evolution in the Scandinavian mountain range is shown in Extended Data Fig. 8). We note that temperature is a more important regulator of ice growth than precipitation, as ‘warm’ summer temperatures can prevent the formation of a perennial snow layer, which is a prerequisite for ice-sheet growth. In fact, precipitation in the Nordic Seas and in northwestern Scandinavia decreases somewhat in the simulations with closed CAA gateways due to the cooler sea surface conditions; changes in precipitation are shown for reference in Extended Data Fig. 9. Therefore, the growth of the incipient ice sheet in Scandinavia in the closed CAA experiments is driven by the weakened AMOC and sea-ice-induced cooling over the eastern North Atlantic.

In these simulations, the total Northern Hemisphere ice-sheet volume grows by around 3 m sea-level equivalent (SLE) in 815 years (about 3.5–4.0 m SLE per millennium), which is consistent with proxy-data evidence of around 3–5 m SLE per millennium in the first part of the last glacial period^{2,3} (Fig. 1a). Importantly, these numbers are substantially smaller than the modern depth of Bering Strait (around 50 m). Hence, assuming that the inception was initiated when the sea level was similar to modern as suggested by proxy data^{2,3}, Bering Strait would have remained open while the

incipient ice sheet was established in the CAA. This is critical, as a closing of Bering Strait eliminates the net freshwater flux from the North Pacific to the North Atlantic, resulting in a warmer and more saline North Atlantic and an invigorated ocean overturning (as shown by refs. 35,36). Hence, a net freshwater transport across Bering Strait is necessary for these feedback processes to sufficiently cool Scandinavia following glacial obstruction of the CAA straits.

Implications for other periods

The response to a closing of Arctic gateways may have implications for the North Atlantic climate conditions and the Scandinavian Ice Sheet evolution (or Eurasian Ice Sheet, more broadly) in other periods beyond the last glacial inception. For example, a recent reconstruction¹⁷ of the Northern Hemisphere ice sheets over the last glacial period indicates that Scandinavia was largely ice free (about 45 ka) during Marine Isotope Stage 3. While large uncertainties exist in this ice-sheet reconstruction, it is suggested that the Scandinavian Ice Sheet minimum and subsequent regrowth was concurrent with a relatively smaller North American ice sheet, largely confined to the southern CAA region^{17,47}. The overall smaller global ice volume during this period (about 30 m SLE (refs. 17,47)) may have re-established North Pacific freshwater transport across Bering Strait (which was a land bridge during much of the last glacial period as water was sequestered in the sub-polar ice sheets), thereby initiating the proposed ocean–atmosphere–cryosphere feedback from the obstructed CAA gateways. The regional cooling of the Nordic Seas and Scandinavia that ensued helped support the rapid regrowth of the Scandinavian Ice Sheet.

Moreover, a recent study⁴⁸ suggests that the inundation of the Bering Strait land bridge in the last deglaciation may have occurred as early as 13.0–13.5 ka. Studies also show that large, coherent ice shelves covered the CAA region until about 11 ka, where the oldest post-glacial marine shells are dated to 11.6 ka (refs. 49). This is intriguing as it suggests that the proposed feedback mechanism may have also contributed to the Younger Dryas (~12.9–11.7 ka) cold reversal that punctuated the overall warming trend of the last deglaciation, during which the Scandinavian Ice Sheet experienced a partial regrowth⁵⁰.

It is thus conceivable that changes in the North Pacific–North Atlantic water exchange through the CAA gateways were an important regulator of North Atlantic cold reversals and the Scandinavian Ice Sheet evolution throughout the Pleistocene. Further studies of these potential links are therefore a high priority for ongoing and future research on remote teleconnections, feedback processes and the climate evolution during glacial periods.

Online content

Any methods, additional references, Nature Research reporting summaries, source data, extended data, supplementary information, acknowledgements, peer review information; details of author contributions and competing interests; and statements of data and code availability are available at <https://doi.org/10.1038/s41561-022-00956-9>.

Received: 15 January 2021; Accepted: 20 April 2022;

Published online: 9 June 2022

References

- Berger, A. et al. Interglacials of the last 800,000 years. *Rev. Geophys.* **54**, 162–219 (2016).
- Kopp, R. E., Simons, F. J., Mitrovica, J. X., Maloof, A. C. & Oppenheimer, M. Probabilistic assessment of sea level during the last interglacial stage. *Nature* **462**, 863–867 (2009).
- Spratt, R. M. & Lisiecki, L. E. A late Pleistocene sea level stack. *Clim. Past* **12**, 1079–1092 (2016).
- Waelbroeck, C. et al. Sea-level and deep water temperature changes derived from benthic foraminifera isotopic records. *Quat. Sci. Rev.* **21**, 295–305 (2002).

5. Lambeck, K. & Chappell, J. Sea level change through the last glacial cycle. *Science* **292**, 679–686 (2001).
6. Govin, A. et al. Persistent influence of ice sheet melting on high northern latitude climate during the early Last Interglacial. *Clim. Past* **8**, 483–507 (2012).
7. Risebrobakken, B., Dokken, T. & Jansen, E. Extent and variability of the meridional Atlantic circulation in the eastern Nordic Seas during Marine Isotope Stage 5 and its influence on the inception of the last glacial. *Geophys. Monogr.* **158**, 323–339 (2005).
8. Risebrobakken, B. et al. Inception of the Northern European ice sheet due to contrasting ocean and insolation forcing. *Quat. Res.* **67**, 128–135 (2007).
9. Zhuravleva, A., Bauch, H. A. & Spielhagen, R. F. Atlantic water heat transfer through the Arctic gateway (Fram Strait) during the Last Interglacial. *Glob. Planet. Change* **157**, 232–243 (2017).
10. Oppo, D. W., McManus, J. F. & Cullen, J. L. Evolution and demise of the Last Interglacial warmth in the subpolar North Atlantic. *Quat. Sci. Rev.* **25**, 3268–3277 (2006).
11. Nørgaard-Pedersen, N., Mikkelsen, N. & Kristoffersen, Y. Arctic Ocean record of last two glacial–interglacial cycles off North Greenland/Ellesmere Island—implications for glacial history. *Mar. Geol.* **244**, 93–108 (2007).
12. Svendsen, J. I. et al. Late Quaternary ice sheet history of northern Eurasia. *Quat. Sci. Rev.* **23**, 1229–1271 (2004).
13. Stokes, C. R., Tarasov, L. & Dyke, A. S. Dynamics of the North American Ice Sheet Complex during its inception and build-up to the Last Glacial Maximum. *Quat. Sci. Rev.* **50**, 86–104 (2012).
14. Kleman, J., Fastook, J. & Stroeven, A. P. Geologically and geomorphologically constrained numerical model of Laurentide Ice Sheet inception and build-up. *Quat. Int.* **95**, 87–98 (2002).
15. Kleman, J., Fastook, J., Ebert, K., Nilsson, J. & Caballero, R. Pre-LGM Northern Hemisphere paleo-ice sheet topography. *Clim. Past* **9**, 2365–2378 (2013).
16. Mangerud, J. in *Klimageschichtliche Probleme der letzten 130 000 Jahre* (ed. Frenzel, B.) 451 (Fischer, Stuttgart, 1991).
17. Batchelor, C. L. et al. The configuration of Northern Hemisphere ice sheets through the Quaternary. *Nat. Commun.* **10**, 3713 (2019).
18. Simon, Q., Hillaire-Marcel, C., St-Onge, G. & Andrews, J. T. North-eastern Laurentide, western Greenland and southern Inuitian ice stream dynamics during the last glacial cycle. *J. Quat. Sci.* **29**, 14–26 (2014).
19. Dong, L. et al. Isotopic fingerprints of ice-rafted debris offer new constraints on mid to late Quaternary Arctic circulation and glacial history. *Geochem. Geophys. Geosyst.* **21**, e2020GC009019 (2020).
20. Barr, I. D. & Clark, C. D. Late Quaternary glaciations in far NE Russia; combining moraines, topography and chronology to assess regional and global glaciation synchrony. *Quat. Sci. Rev.* **53**, 72–87 (2012).
21. Tulenko, J. P., Lofverstrom, M. & Briner, J. P. Ice sheet influence on atmospheric circulation explains the patterns of Pleistocene alpine glacier records in North America. *Earth Planet. Sci. Lett.* **534**, 116115 (2020).
22. Lofverstrom, M., Liakka, J. & Kleman, J. The North American Cordillera—an impediment to growing the continent-wide Laurentide Ice Sheet. *J. Clim.* **28**, 9433–9450 (2015).
23. Lofverstrom, M. & Liakka, J. On the limited ice intrusion in Alaska at the LGM. *Geophys. Res. Lett.* **43**, 11030–11038 (2016).
24. Liakka, J., Lofverstrom, M. & Colleoni, F. The impact of the North American glacial topography on the evolution of the Eurasian ice sheet over the last glacial cycle. *Clim. Past* **12**, 1225–1241 (2016).
25. Liakka, J. & Lofverstrom, M. Arctic warming induced by the Laurentide Ice Sheet topography. *Clim. Past* **14**, 887–900 (2018).
26. Seager, R. et al. Is the Gulf Stream responsible for Europe's mild winters? *Q. J. R. Meteorol. Soc.* **128**, 2563–2586 (2002).
27. Rossby, T. The North Atlantic Current and surrounding waters: at the crossroads. *Rev. Geophys.* **34**, 463–481 (1996).
28. Kleman, J. et al. North American Ice Sheet build-up during the last glacial cycle, 115–21 kyr. *Quat. Sci. Rev.* **29**, 2036–2051 (2010).
29. Kohfeld, K. E., Fairbanks, R. G., Smith, S. L. & Walsh, I. D. *Neogloboquadrina pachyderma* (sinistral coiling) as paleoceanographic tracers in polar oceans: evidence from northeast water polynya plankton tows, sediment traps, and surface sediments. *Paleoceanography* **11**, 679–699 (1996).
30. McManus, J. F., Oppo, D. W., Keigwin, L. D., Cullen, J. L. & Bond, G. C. Thermohaline circulation and prolonged interglacial warmth in the North Atlantic. *Quat. Res.* **58**, 17–21 (2002).
31. Kuhlbrodt, T. et al. On the driving processes of the Atlantic meridional overturning circulation. *Rev. Geophys.* **45**, RG2001 (2007).
32. Lozier, M. S. et al. A sea change in our view of overturning in the subpolar North Atlantic. *Science* **363**, 516–521 (2019).
33. Carmack, E. C. The alpha/beta ocean distinction: a perspective on freshwater fluxes, convection, nutrients and productivity in high-latitude seas. *Deep Sea Res.* **2** **54**, 2578–2598 (2007).
34. Aagaard, K. & Carmack, E. C. The role of sea ice and other fresh water in the Arctic circulation. *J. Geophys. Res. Oceans* **94**, 14485–14498 (1989).
35. Otto-Bliesner, B. L. et al. Amplified North Atlantic warming in the late Pliocene by changes in Arctic gateways. *Geophys. Res. Lett.* **44**, 957–964 (2016).
36. Hu, A. et al. Influence of Bering Strait flow and North Atlantic circulation on glacial sea-level changes. *Nat. Geosci.* **3**, 118–121 (2010).
37. Karami, M. P., Myers, P. G., de Vernal, A., Tremblay, L. B. & Hu, X. The role of Arctic gateways on sea ice and circulation in the Arctic and North Atlantic oceans: a sensitivity study with an ocean-sea-ice model. *Clim. Dyn.* **57**, 2129–2151 (2021).
38. Woodgate, R. A., Aagaard, K. & Weingartner, T. J. Monthly temperature, salinity, and transport variability of the Bering Strait through flow. *Geophys. Res. Lett.* **32**, L04601 (2005).
39. Münchow, A., Falkner, K. K. & Melling, H. Baffin Island and west Greenland current systems in northern Baffin Bay. *Prog. Oceanogr.* **132**, 305–317 (2015).
40. Prinsenberg, S. & Hamilton, J. Monitoring the volume, freshwater and heat fluxes passing through Lancaster Sound in the Canadian Arctic Archipelago. *Atmos. Ocean* **43**, 1–22 (2005).
41. Danabasoglu, G. et al. The Community Earth System Model version 2 (CESM2). *J. Adv. Model. Earth Syst.* **12**, e2019MS001916 (2020).
42. Vettoretti, G. & Peltier, W. Post-Eemian glacial inception. Part I: the impact of summer seasonal temperature bias. *J. Clim.* **16**, 889–911 (2003).
43. Jochum, M. et al. True to Milankovitch: glacial inception in the new Community Climate System Model. *J. Clim.* **25**, 2226–2239 (2012).
44. Birch, L., Cronin, T. & Tziperman, E. Glacial inception on Baffin Island: the role of insolation, meteorology, and topography. *J. Clim.* **30**, 4047–4064 (2017).
45. Born, A., Kageyama, M. & Nisancioglu, K. Warm Nordic Seas delayed glacial inception in Scandinavia. *Clim. Past* **6**, 817–826 (2010).
46. Guihou, A. et al. Enhanced Atlantic meridional overturning circulation supports the last glacial inception. *Quat. Sci. Rev.* **30**, 1576–1582 (2011).
47. Gowan, E. J. et al. A new global ice sheet reconstruction for the past 80 000 years. *Nat. Commun.* **12**, 1199 (2021).
48. Pico, T., Mitrovica, J. & Mix, A. Sea level fingerprinting of the Bering Strait flooding history detects the source of the Younger Dryas climate event. *Sci. Adv.* **6**, eaay2935 (2020).
49. England, J. et al. The Inuitian Ice Sheet: configuration, dynamics and chronology. *Quat. Sci. Rev.* **25**, 689–703 (2006).
50. Mangerud, J. et al. A major re-growth of the Scandinavian Ice Sheet in western Norway during Allerød–Younger Dryas. *Quat. Sci. Rev.* **132**, 175–205 (2016).
51. Petit, J.-R. et al. Climate and atmospheric history of the past 420,000 years from the Vostok ice core, Antarctica. *Nature* **399**, 429–436 (1999).

Publisher's note Springer Nature remains neutral with regard to jurisdictional claims in published maps and institutional affiliations.

© The Author(s), under exclusive licence to Springer Nature Limited 2022

Methods

CESM2. The simulations described in this paper are conducted with Community Earth System Model, version 2 (CESM2)⁴¹, which is a contemporary high-complexity, coupled, global Earth-system model consisting of prognostic components of atmosphere, land, river, ocean, sea ice and land ice.

One of the major novelties in CESM2 is the inclusion of a two-way interactive, thermo-mechanical ice-sheet component (Community Ice Sheet Model, version 2 (CISM2⁵³)) with a high-order velocity solver. The CESM2–CISM2 coupling is described in detail in ref. ⁵³; a brief summary of the most important features relevant for this study is provided in the following.

The ice-sheet mass balance is determined by mass input from accumulation of snow and mass loss from surface melting and run-off (fraction of liquid water that is not refrozen in the snow pack), basal melting, iceberg calving and sublimation⁵⁴. The surface mass balance (accumulation and surface melt) is calculated on multiple elevation classes in the land component of CESM2 using an energy-based mass-balance scheme to represent realistic spatio-temporal variations in accumulation and ablation. Snow accumulation that exceeds the maximum allowed snow depth (10 m liquid water equivalent) is added to the top of the snow pack, and an equivalent amount is removed from the bottom of the snow pack and converted to a positive surface mass balance. The surface mass balance is subsequently downscaled to the ice-sheet model grid using a conservative interpolation method that ensures that the total accumulation and ablation are the same on both model grids⁵³.

The ice-sheet model also sends freshwater from basal melting (liquid run-off) and calving fluxes (solid discharge) directly to the ocean component of CESM2. The ocean model melts the calving flux instantaneously (no iceberg model is currently included) using energy from the global ocean to suppress numerical instabilities that may arise if the melt energy came from a single ocean grid cell. The temperature and salinity anomalies from the implied freshwater fluxes are spread diffusively in the surface ocean using a normal distribution with a maximum radius of 300 km from the coast.

The distribution of vegetation (bare soil plus 15 different vegetation types) is prescribed in each land-model grid cell, but ecosystem dynamics (life cycle and mortality) are prognostic. Land surface types (glaciated, vegetated and lakes/wetland) are also dynamic to accommodate the transition between different surface conditions as the simulated ice sheets expand.

All simulations were run on the default, nominal 1° resolution grids: the atmosphere and land components use a uniform 0.9° × 1.25° (latitude × longitude) finite volume grid, where the former has 32 terrain-following hybrid sigma-pressure levels in the vertical, and a model top at 2.26 hPa (about 40 km). The ocean and sea-ice components share a grid with spherical coordinates in the Southern Hemisphere and a displaced pole grid in the Northern Hemisphere where the North Pole is located over Greenland. This grid has a nominal 1.125° resolution in the zonal direction and varying resolution in the meridional direction, with a grid spacing of as high as 0.38° around Greenland (a nominal resolution of about 40 km). The ocean model has 60 levels in the vertical, with a uniform 10 m resolution in the upper 160 m, followed by a transition zone where the vertical grid spacing increases monotonically to a maximum of 250 m at depths below 3,500 m; the minimum and maximum resolved depths are 30 m and 5,500 m, respectively. Finally, the ice-sheet component adopts a 4 × 4 km horizontal resolution. The high spatial resolution enables a detailed representation of topography, which is essential for capturing inception regions that often occur in high-elevation areas. The ice-sheet model was configured to run synchronously with the other Earth-system model components (CISM2 advances one year for every CESM2 year) to ensure conservation of freshwater, salinity and energy.

CESM2 settings and model-specific caveats. The model simulations described in this paper adopted default (out-of-the-box) CESM2 settings, except for a few modifications described in this section; all of these modifications were toggled by name-list changes, and no changes were made to the model source code.

Ice-sheet model. In the default configuration of CESM2, the ice-sheet component runs on a limited area grid centred over Greenland. To facilitate experiments of high-latitude glacial inception, the CISM2 model domain was extended to encompass a large fraction of the Northern Hemisphere continents and oceans (Fig. 2); the extended ice-sheet model grid has 2,592 × 2,592 grid cells and matches the 4 × 4 km resolution of the ‘Greenland grid’ (indicated in Fig. 2) currently supported in CESM2. The topography is based on the GMTED2010⁵⁵ dataset (Global Multi-resolution Terrain Elevation Data 2010) at approximately 1 km resolution (30 arc-second resolution), and bathymetry is derived from the ETOPO1⁵⁶ dataset at approximately 2 km resolution (1 arc-minute resolution).

The ice-sheet model was run with an active isostasy model, with an elastic lithosphere and relaxing asthenosphere (with a relaxation timescale of 3,000 years). The bedrock topography was initialized from a relaxed state in equilibrium, derived from the global GMTED2010 dataset at approximately 1 km resolution.

The calving parameterization was configured to allow floating (or grounded) ice shelves to form where the ocean depth is less than 600 m; ice is instantaneously calved where the ocean depth is greater than this value. This crude parameterization mimics the default model behaviour, where ice is

instantaneously calved when it becomes afloat (ocean depth is greater than 0 m). The 600 m limit was selected to allow marine ice to form in regions with known ice shelves in the last glacial period, including the CAA region and in Barents and Kara seas (Fig. 2). The results may be somewhat sensitive to the crudeness of the calving parameterization, and we note that a more realistic representation of both ice shelves (floating and grounded) and calving processes are ongoing areas of development in CESM.

Glacial inception occurs in areas where the 10 m maximum snow depth is exceeded in the land model. All ice that is simulated on the ice-sheet model grid (Fig. 2) is dynamically active when the thickness is 1 m or greater. This also includes the Greenland Ice Sheet that is fully interactive and dynamically evolving in these simulations. However, for plotting purposes and to better highlight the inception and early ice-sheet growth in Fig. 4, we indicate the initial extent of the Greenland Ice Sheet in grey shading (see also Extended Data Fig. 3).

Atmosphere model. The atmosphere model is configured to include period-appropriate radiative boundary conditions for 116 ka. This includes changes in Earth’s orbital parameters and the concentration^{51,57} of atmospheric CO₂ (273 parts per million by volume (ppmv)), CH₄ (600 parts per billion by volume (ppbv)) and N₂O (255 ppbv).

The topographic boundary condition used by the atmosphere model is updated transiently as the model runs using the offline method described in ref. ⁵⁸. In short, the ice-sheet topography is extracted from the CISM2 restart file, regridded and overlaid onto the nominal 1 km resolution global GMTED2010 dataset, which forms the basis for the CESM2 topography⁵⁵. The topography generation routine⁵⁹ is then run, which includes remapping of the modified high-resolution topography to a 3 km cubed sphere grid, on which sub-gridscale topography variance and ridge orientations are derived. The topography is then smoothed and interpolated back to the nominal 1° atmosphere model grid, and the new global topography fields are reinserted into the CESM2 boundary conditions. However, as explained in ref. ⁵⁸, updating the model topography at run time is currently not practical as information is derived from high-resolution global datasets using algorithms that are not included or optimized for run-time CESM2 operation. As such, execution time of the topography updating routine is comparable to the integration time of several CESM2 years. We therefore executed the topography updating routine in parallel with CESM2, and the topographic boundary condition in the atmosphere model was updated with a 5 yr lag compared with the ice-sheet component. This is a reasonable compromise since year-to-year changes in ice-sheet elevation are small compared with the background topography. Albedo affects of the changing ice sheets are, however, accounted for at run time through dynamically evolving land surface types in the land model.

Land model. The vegetation distribution is a potentially limiting factor in these experiments. Since no global vegetation reconstructions exist for the 116 ka period, we prescribed a pre-industrial, non-anthropogenic vegetation distribution (no crops or urban areas), which is the vegetation boundary condition used in the Last Interglacial simulations in phase 4 of the Paleoclimate Modelling Intercomparison Project⁶⁰. While this is a sensible first-order approximation of the vegetation distribution, tundra and cold resistant vegetation types probably migrated to more southern latitudes during the inception period, which may have influenced the local climate conditions and thus impacted where perennial snow layers can be established. Exploring the sensitivity to the vegetation distribution would require the development of a proxy-data validated, global vegetation distribution for this specific period. We therefore leave the exploring of this sensitivity to future work.

Ocean model. Perhaps the most important limitation of CESM2 for these experiments is that the global ocean has a constant volume, and freshwater fluxes are treated as virtual salt fluxes using a constant reference salinity. Changes in eustatic sea level are thus implicitly accounted for through ocean salinity adjustments; however, the global integral of the ocean volume (and land–ocean boundary) remains constant even when large volumes of water are sequestered on land in growing ice sheets. However, the implied global sea-level change from the growing ice sheets is only about 3 m (as described), which is substantially smaller than the 30 m minimum allowed ocean depth and is thus too small to be resolved by the model. Nevertheless, the spatially resolved local sea surface height (local sea level) is variable and depends on ocean circulation, heat content and salinity anomalies.

A more important limitation of the prescribed land–ocean boundary is that ocean gateways remain open even if they are covered (let alone completely filled) by an overriding ice sheet. To accommodate for this limitation, we conducted two long (multi-century) simulations with CESM2: (1) in the first simulation, the CAA gateways were left open (the same land–ocean configuration as in the pre-industrial simulation), and (2) in the second simulation, the land–ocean domain files were modified to close the CAA gateways to emulate the physical obstruction by a marine ice sheet (note that only a handful of ocean grid cells were modified as shown in see Extended Data Fig. 2). Comparison between these twin simulations therefore permits an assessment of the sensitivity to water exchange between the Arctic and the North Atlantic through the CAA gateways.

Model simulations. Three model simulations are compared in this study, a long pre-industrial control simulation and two simulations with a 116 ka forcing protocol and either open or closed ocean gateways in the CAA region.

Pre-industrial control simulation. The pre-industrial simulation is described in detail in ref. ⁴¹, which is the official CESM2 control simulation for the Coupled Modelling Intercomparison Project, version 6 (CMIP6). This simulation reflects an 'unforced' model state in statistical equilibrium—the long-term climate drift is negligible compared with interannual variability—and all intercomponent fluxes, states, interactions and feedbacks are in internal balance. The control simulation consists of a 1,200-year-long integration of CESM2 under the constant CMIP6 ce1850 forcing protocol⁴¹. Note that this simulation was run with a prescribed Greenland Ice Sheet that interacts with the circulation through topography, albedo and surface snow effects, but it does not respond itself to the simulated climate. Climatologies are formed over model years 1170–1200, using a standard climatological period of three decades.

116 ka simulation with open CAA gateways. The default 116 ka simulation uses the modern observed land–ocean distribution (including open CAA gateways) and the time appropriate orbital configuration and greenhouse gas concentrations described in the preceding. This simulation also adopted the extended ice-sheet model grid (Fig. 2) to simulate inception and early ice-sheet growth over the Northern Hemisphere continents.

The model climate was initiated from the spun-up pre-industrial climate/Greenland Ice Sheet simulation described in ref. ³⁸. The climate in this simulation is comparable to the pre-industrial simulation in CMIP6⁴¹ (described in the preceding), but quantitative differences in the sea surface temperature exist around Greenland that are attributed to the presence of a dynamic ice-sheet model.

With the exception of the spun-up Greenland Ice Sheet and the Antarctic Ice Sheet (the latter was prescribed at its modern geometry), all other glaciers and ice caps were removed and replaced with bare-ground initial conditions. Snow layers were also removed and added to the global ocean to eliminate local surface albedo and thermal effects that may bias ice growth in areas that have perennial snow layers in the modern climate. The simulation was run for a total of 815 years under a constant 116 ka forcing protocol, and climatologies were formed over model years 785–815 (the last 30 years of the simulation).

116 ka simulation with closed CAA gateways. The sensitivity simulation with closed CAA gateways is identical to the simulation with open CAA gateways described in the preceding. The only difference is that a handful of grid cells in the CAA region were changed from ocean to land in the lateral domains of the land and ocean models (Extended Data Fig. 2). These changes are sufficient to completely close the CAA gateways (thus emulating the physical obstruction of a thick ice shelf) and thereby turn off the Arctic–North Atlantic water exchange through the archipelago. As part of the model initialization process, CESM2 automatically assigns ice (glacier land units) to these new land-model grid cells to match the glacier extent in the ice-sheet model.

The simulation was branched from year 500 of the 116 ka simulation with open CAA gateways, and it was run for 315 years from the branch point. This means that both the open CAA and closed CAA simulations ended at nominal model year 815 from initialization. Similar to the open CAA simulation, climatologies were formed over model years 785–815 (the last 30 years of the simulation).

Proxy data. Reconstructions of North Atlantic climate and oceanographic conditions during the last glacial inception were obtained from public repositories of previously published palaeoclimate data in the Pangaea database. We follow the interpretations of the original authors, based on the local calibration of the proxies with oceanographic conditions. In particular, we leverage sea surface temperatures and the percentage abundance and $\delta^{13}\text{C}$ signature of cold-water planktonic foraminifera (left/sinistral coiling *Neogloboquadrina pachyderma*) as proxies for the relative contribution of Arctic waters (higher *N. pachyderma* abundance and more positive $\delta^{13}\text{C}$) and North Atlantic waters (lower abundance and more negative $\delta^{13}\text{C}$) as a function of changes in AMOC strength^{6–8}. Moreover, the number of IRDs—terrigenous material with grain size larger than 0.5 mm—per gram of sediment was utilized as a proxy for the regional presence of marine terminating and dynamically active ice sheets. Finally, global sea-level variations are derived from ref. ³, insolation variations are obtained from ref. ¹ and the time series of atmospheric CO_2 is derived from the Vostok ice core⁵¹.

Data availability

CESM2 data from the pre-industrial and 116 ka simulations with open and closed CAA gateways are available via Zenodo: <https://doi.org/10.5281/zenodo.6563697>. Original repositories for the pre-industrial simulation and proxy datasets may be

found at https://www.earthsystemgrid.org/dataset/ucar.cgd.cesm2.b.e21.B1850.f09_g17.CMIP6-piControl.001.html, vo.imcce.fr/insola/earth/online/earth/earth.html, <https://doi.org/10.1594/PANGAEA.854045>, <https://doi.org/10.1594/PANGAEA.55501>, <https://doi.org/10.1594/PANGAEA.840727>, <https://doi.org/10.1594/PANGAEA.777694>, <https://doi.org/10.1594/PANGAEA.742858>.

Code availability

The simulations in this study were produced with the publicly released version of CESM2.1.1, which is open-source software, freely available at <http://www.cesm.ucar.edu/>.

References

- Lipscomb, W. et al. Description and evaluation of the Community Ice Sheet Model (CISM) v2.1. *Geosci. Model Dev.* **12**, 387–424 (2019).
- Muntjewerf, L. et al. Description and demonstration of the coupled Community Earth System Model v2–Community Ice Sheet Model v2 (cesm2–cism2). *J. Adv. Model. Earth Syst.* **13**, e2020MS002356 (2021).
- Fyke, J. G., Sergienko, O., Lofverstrom, M., Price, S. & Lenaerts, J. T. An overview of interactions and feedbacks between ice sheets and the Earth system. *Rev. Geophys.* **56**, 361–408 (2018).
- Danielson, J. J. & Gesch, D. B. *Global Multi-Resolution Terrain Elevation Data 2010 (GMTED2010)* Open File Report 2011-1073 (USGS, 2011).
- Amante, C. & Eakins, B. W. *ETOPO1 Arc-Minute Global Relief Model: Procedures, Data Sources and Analysis* Technical Memorandum NESDIS NGDC-24 (NOAA, 2009).
- Spahni, R. et al. Atmospheric methane and nitrous oxide of the late Pleistocene from Antarctic ice cores. *Science* **310**, 1317–1321 (2005).
- Lofverstrom, M. et al. An efficient ice-sheet/Earth system model spin-up procedure for CESM2.1 and CISM2.1: description, evaluation, and broader applicability. *J. Adv. Model. Earth Syst.* **12**, e2019MS001984 (2020).
- Lauritzen, P. H., Bacmeister, J. T., Callaghan, P. F. & Taylor, M. A. NCAR global model topography generation software for unstructured grids. *Geosci. Model Dev.* **8**, 3975–3986 (2015).
- Otto-Bleisner, B. L. et al. The PMIP4 contribution to CMIP6—part 2: two interglacials, scientific objective and experimental design for Holocene and Last Interglacial simulations. *Geosci. Model Dev.* **10**, 3979–4003 (2017).
- Dee, D. P. et al. The ERA-Interim reanalysis: configuration and performance of the data assimilation system. *Q. J. R. Meteorol. Soc.* **137**, 553–597 (2011).

Acknowledgements

The CESM project is supported primarily by the National Science Foundation (NSF). This material is based on work supported by the National Center for Atmospheric Research (NCAR), which is a major facility sponsored by the National Science Foundation under Cooperative Agreement no. 1852977. Computing and data storage resources, including the Cheyenne supercomputer (<https://doi.org/10.5065/D6RX99HX>), were provided by the Computational and Information Systems Laboratory (CISL) at NCAR. The authors extend a special thanks to both the CESM Land Ice Working Group (LIWG) and the Paleoclimate Working Group (PaleoWG) for donating computer time to extend these simulations beyond their original length.

Author contributions

M.L. conceptualized the project, developed boundary conditions, ran the simulations, analysed output data and wrote the original draft of the manuscript. D.M.T. helped with interpretation of proxy data and wrote the corresponding section in the manuscript. B.L.O.-B. helped finance parts of the project. E.C.B. helped develop the ocean boundary conditions for the closed gateways experiment. All authors commented on the final draft.

Competing interests

The authors declare no competing interests.

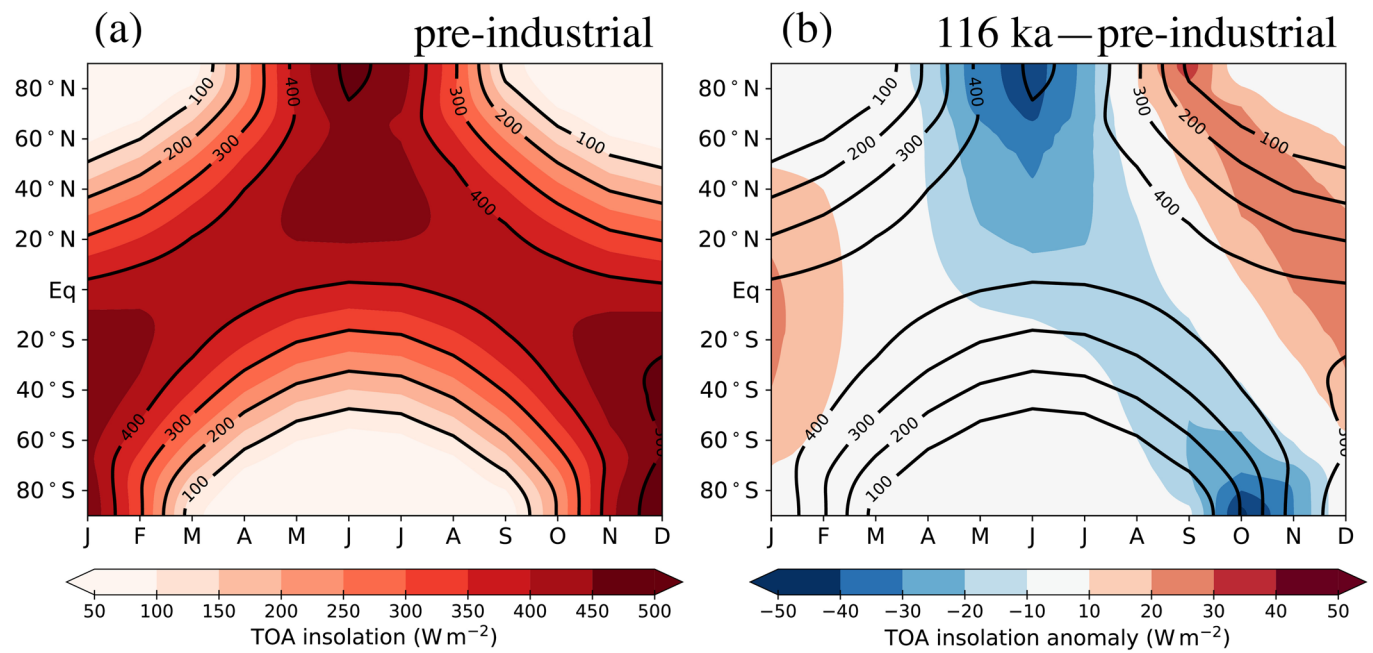
Additional information

Extended data is available for this paper at <https://doi.org/10.1038/s41561-022-00956-9>.

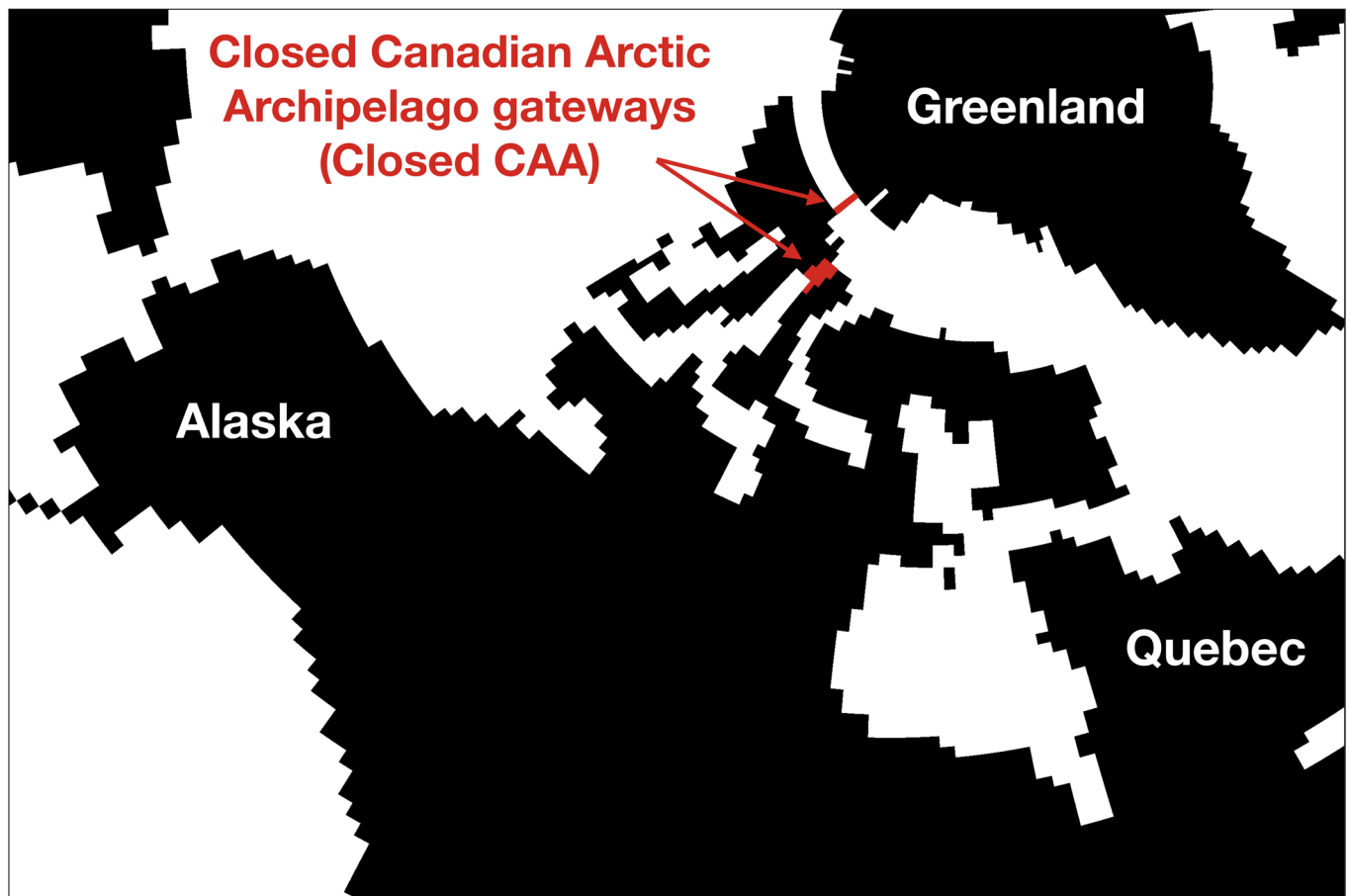
Correspondence and requests for materials should be addressed to Marcus Lofverstrom.

Peer review information *Nature Geoscience* thanks Evan Gowan, Chris R Stokes and the other, anonymous, reviewer(s) for their contribution to the peer review of this work. Primary Handling Editor: James Super, in collaboration with the *Nature Geoscience* team.

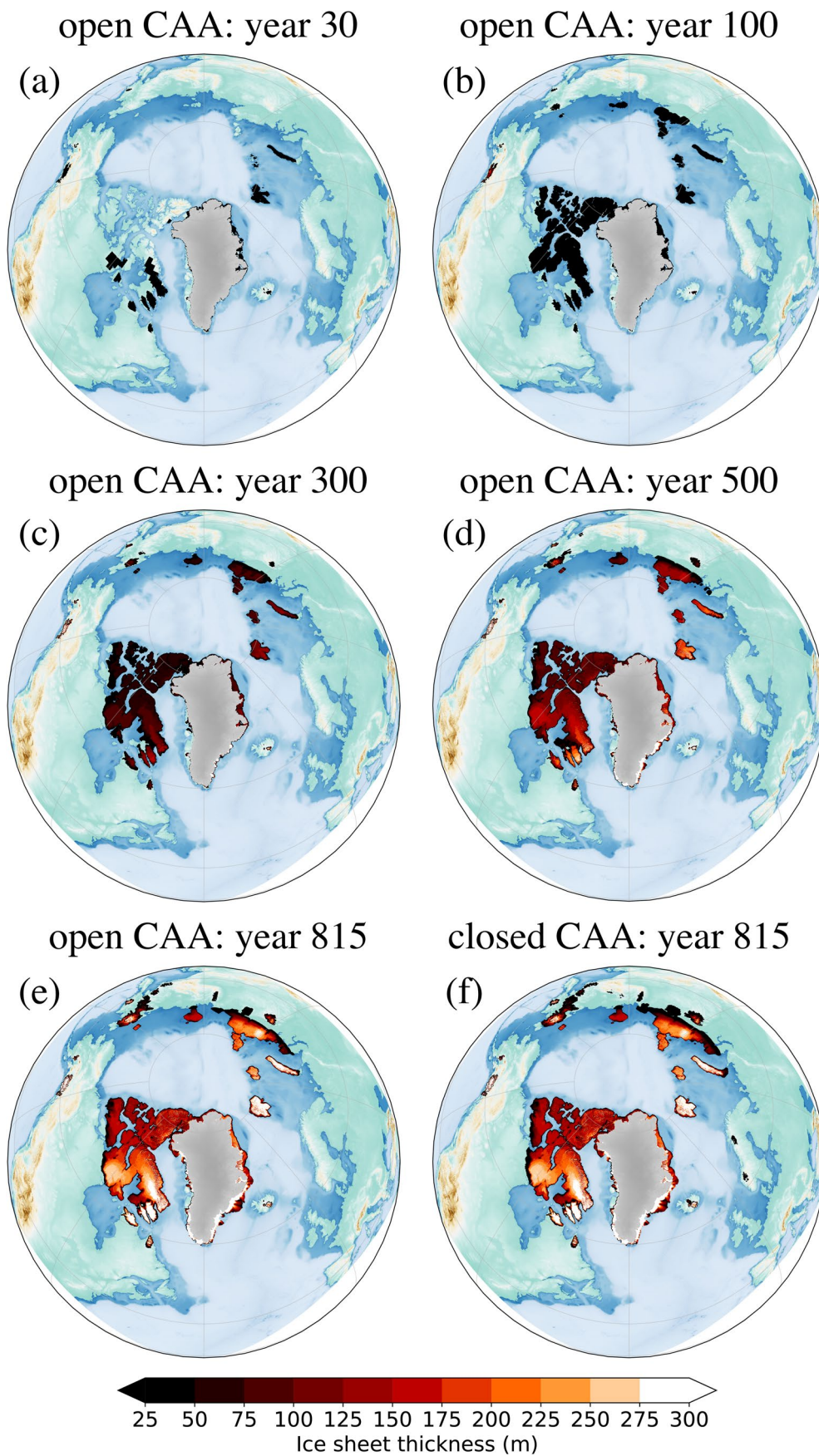
Reprints and permissions information is available at www.nature.com/reprints.



Extended Data Fig. 1 | Latitudinal variations in top-of-atmosphere insolation as a function of month of year. (a) full pre-industrial (1850 CE) top-of-atmosphere insolation, and (b) difference in top-of-atmosphere insolation between the 116 ka and pre-industrial orbital configurations. Contour lines in panel b replicate the contour lines of the full pre-industrial insolation in panel a.

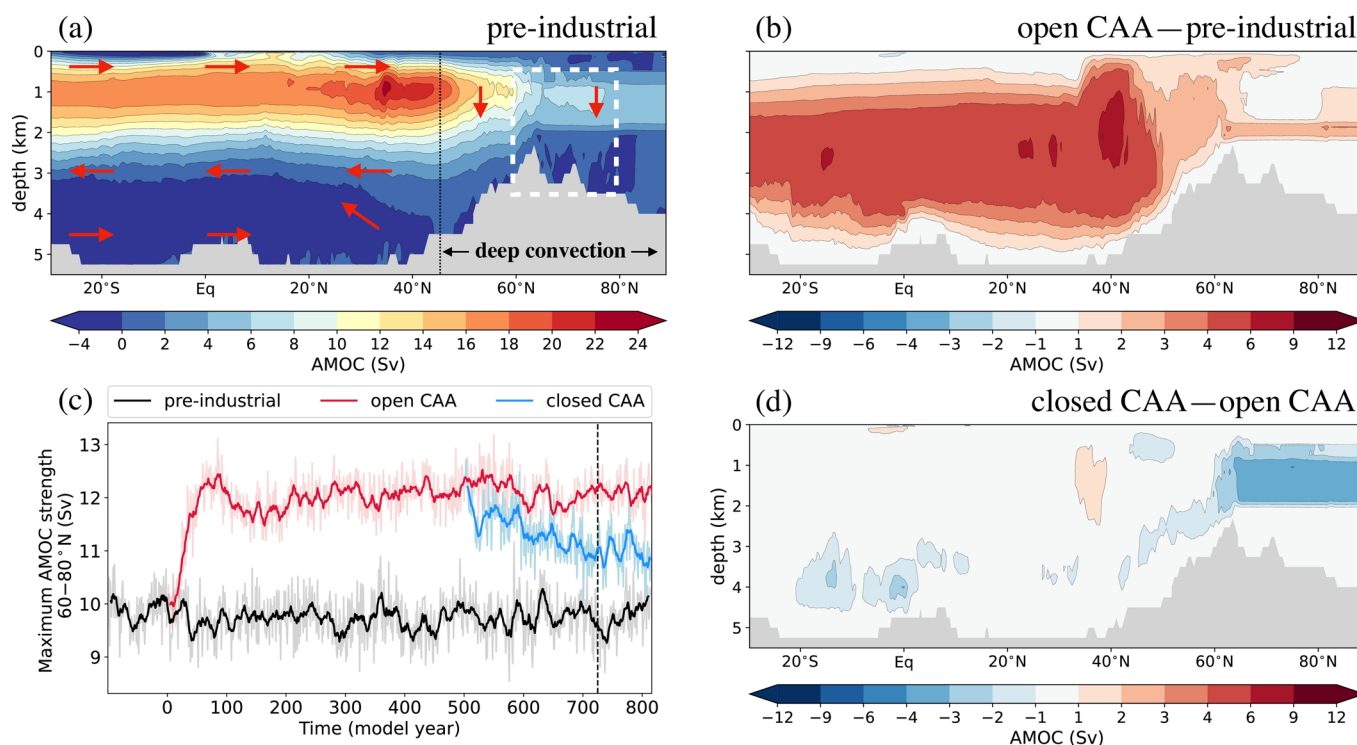


Extended Data Fig. 2 | Map of land-ocean distribution on the ocean-model grid. Land and ocean grid points are indicated by white and black colour, respectively. Grid points that are switched from ocean to land in the closed CAA simulation are indicated by red colour. The background map is showing the land-ocean boundary on the nominal 1-degree ocean model grid.



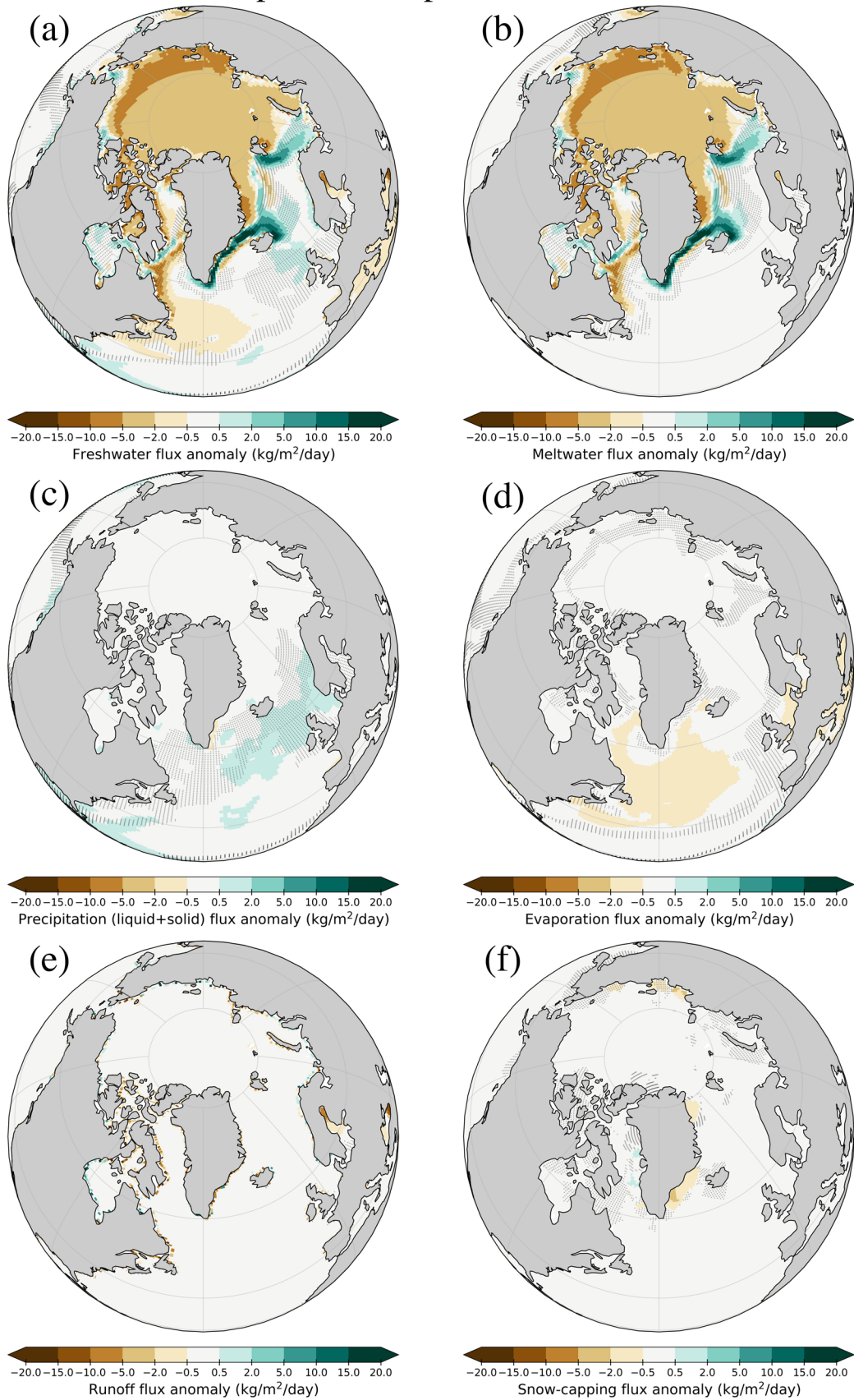
Extended Data Fig. 3 | See next page for caption.

Extended Data Fig. 3 | Spatial and temporal evolution of Northern Hemisphere ice sheets. Panels a-e show the ice evolution in the simulation with open CAA gateways at model year (a) 30, (b) 100, (c) 300, (d) 500, and (e) 815 (the latter is the same as Fig. 4a). Panel (f) shows the corresponding Northern Hemisphere ice distribution at model year 815 in the simulation with closed CAA gateways (same as Fig. 4c) where ice has started forming in the Scandinavian mountains. The background map is showing topography and bathymetry as represented on the 4-km ice-sheet model grid. In the simulation with closed CAA gateways, inception occurs after 725 model years in the high-elevation regions of southern Norway and after 739 model years in northern Norway (see also Extended Data Fig. 8).



Extended Data Fig. 4 | Spatial and temporal evolution of the Atlantic Meridional Overturning Circulation (AMOC). (a) 30 year annual average AMOC from the pre-industrial control simulation (arrows indicate the flow direction); (b) difference between the 116 ka simulation with open CAA gateways and the pre-industrial simulation; (d) difference between the 116 ka simulations with closed and open CAA gateways. Panel (c) shows the temporal evolution of the maximum overturning strength between 60°N and 80°N (white box in panel a) in the pre-industrial (black), open CAA (red), and closed CAA (blue) simulations, respectively.

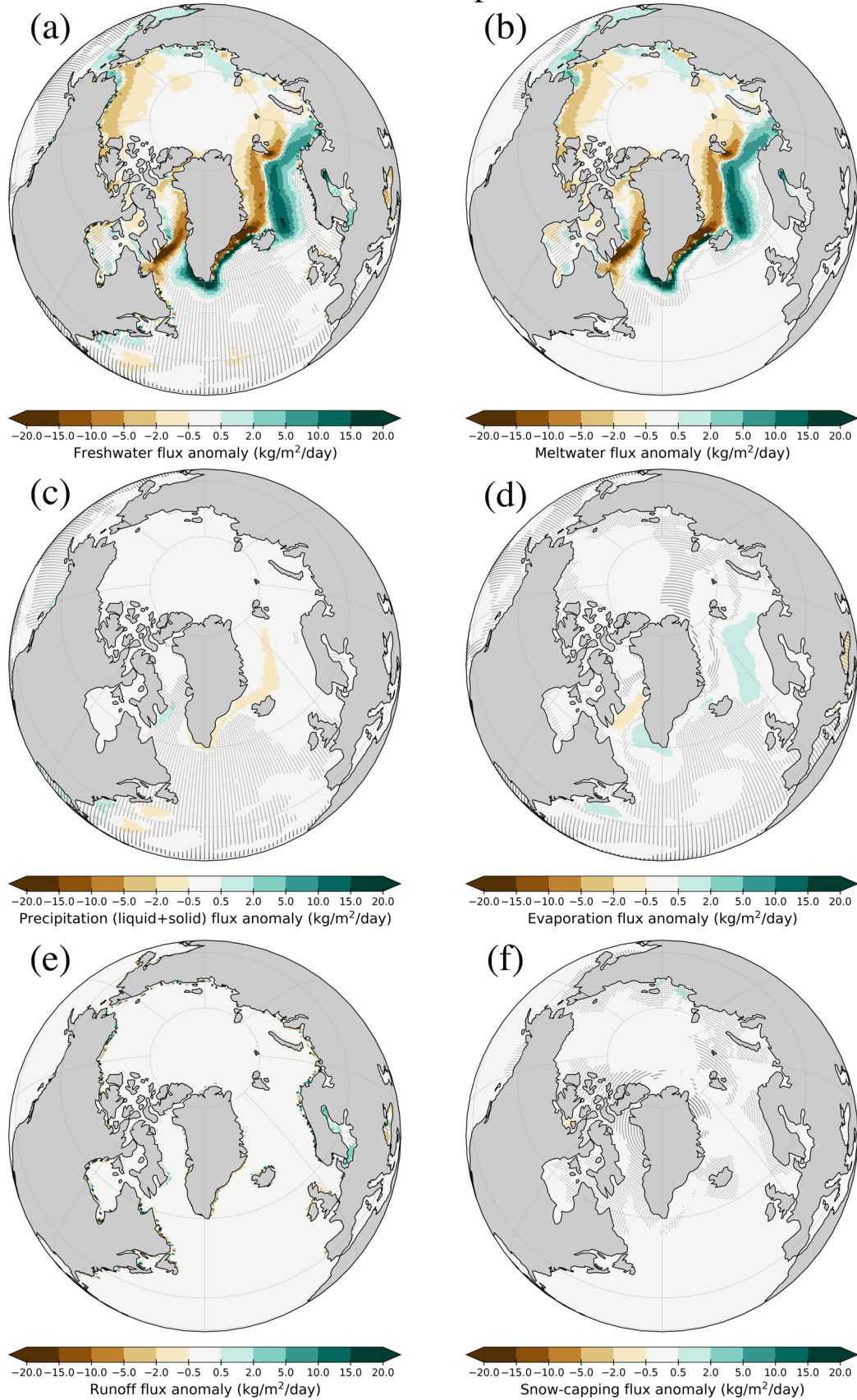
open CAA — pre-industrial



Extended Data Fig. 5 | See next page for caption.

Extended Data Fig. 5 | Differences in surface ocean freshwater budget between the open CAA and the pre-industrial control simulation. (a) Difference in total freshwater flux (sum of panels b-f; same as Fig. 3b) and the contribution from: (b) meltwater fluxes from seasonal sea ice melting, (c) precipitation, (d) evaporation, (e) river transport, and (f) snow capping. Stippling indicates differences that are not significant at the 95% level. Mapping software: Cartopy with Natural Earth shapefiles.

closed CAA—open CAA

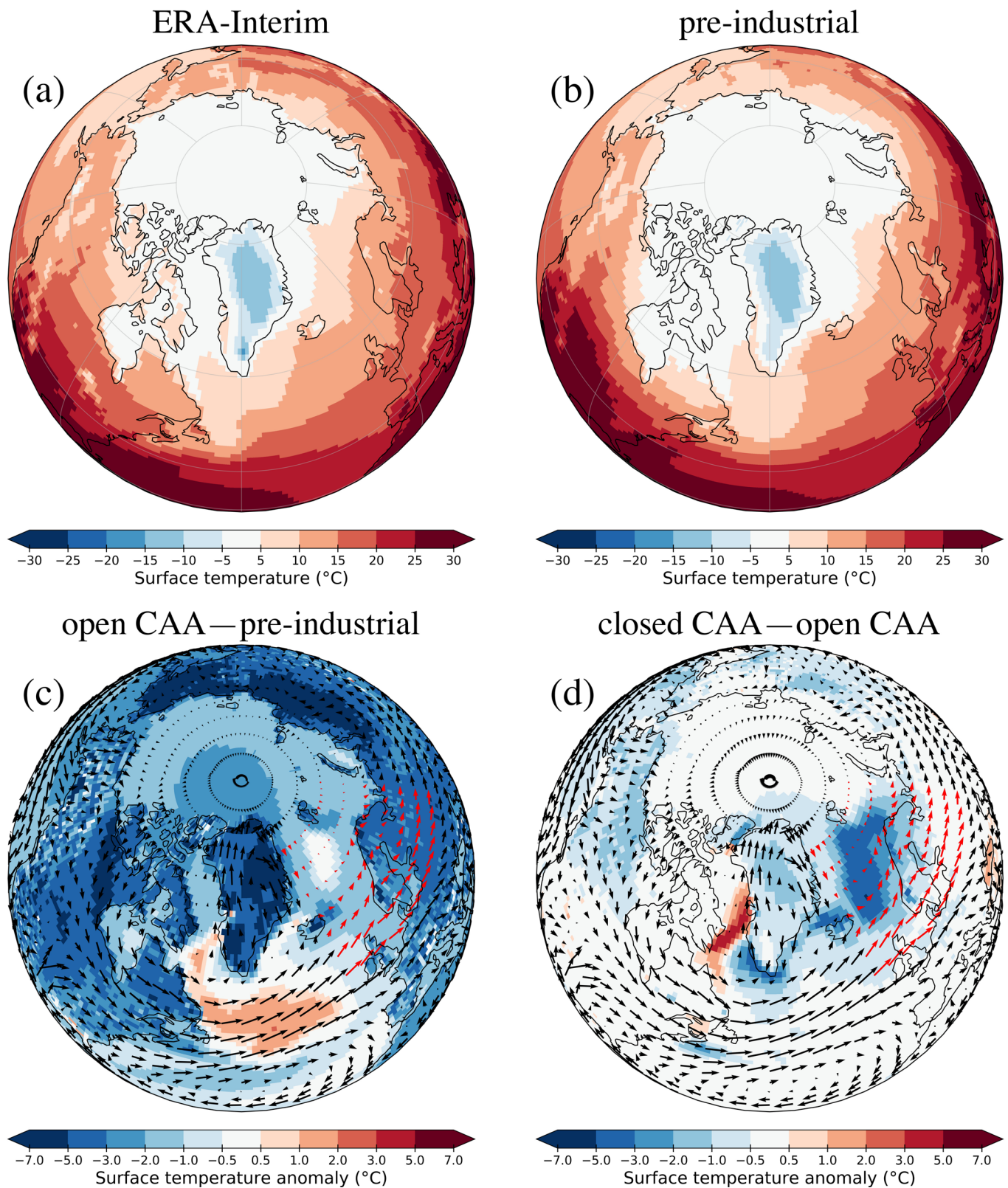


Extended Data Fig. 6 | See next page for caption.

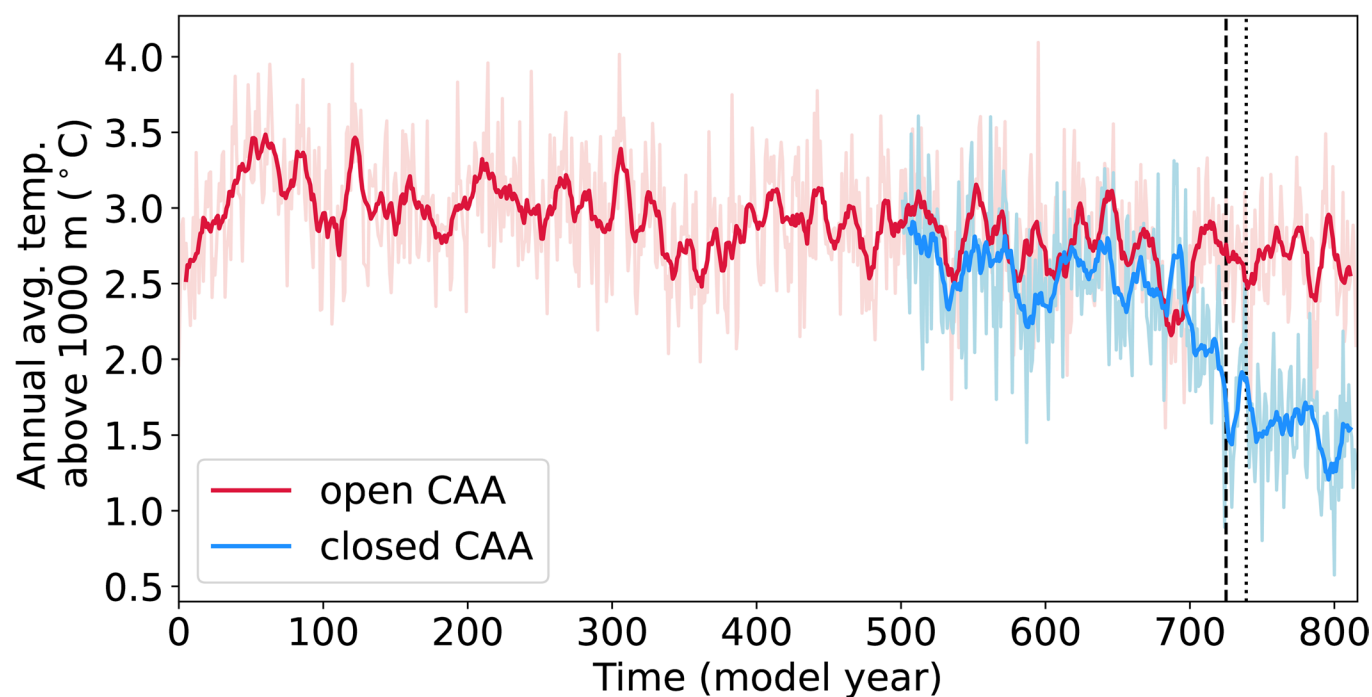
Extended Data Fig. 6 | Differences in surface ocean freshwater budget between the 116 ka simulations with closed and open CAA gateways.

(a) Difference in total freshwater flux (sum of panels b-f; same as Fig. 3e) and the contribution from: (b) meltwater fluxes from seasonal sea ice melting, (c) precipitation, (d) evaporation, (e) river transport, and (f) snow capping. Stippling indicates differences that are not significant at the 95% level.

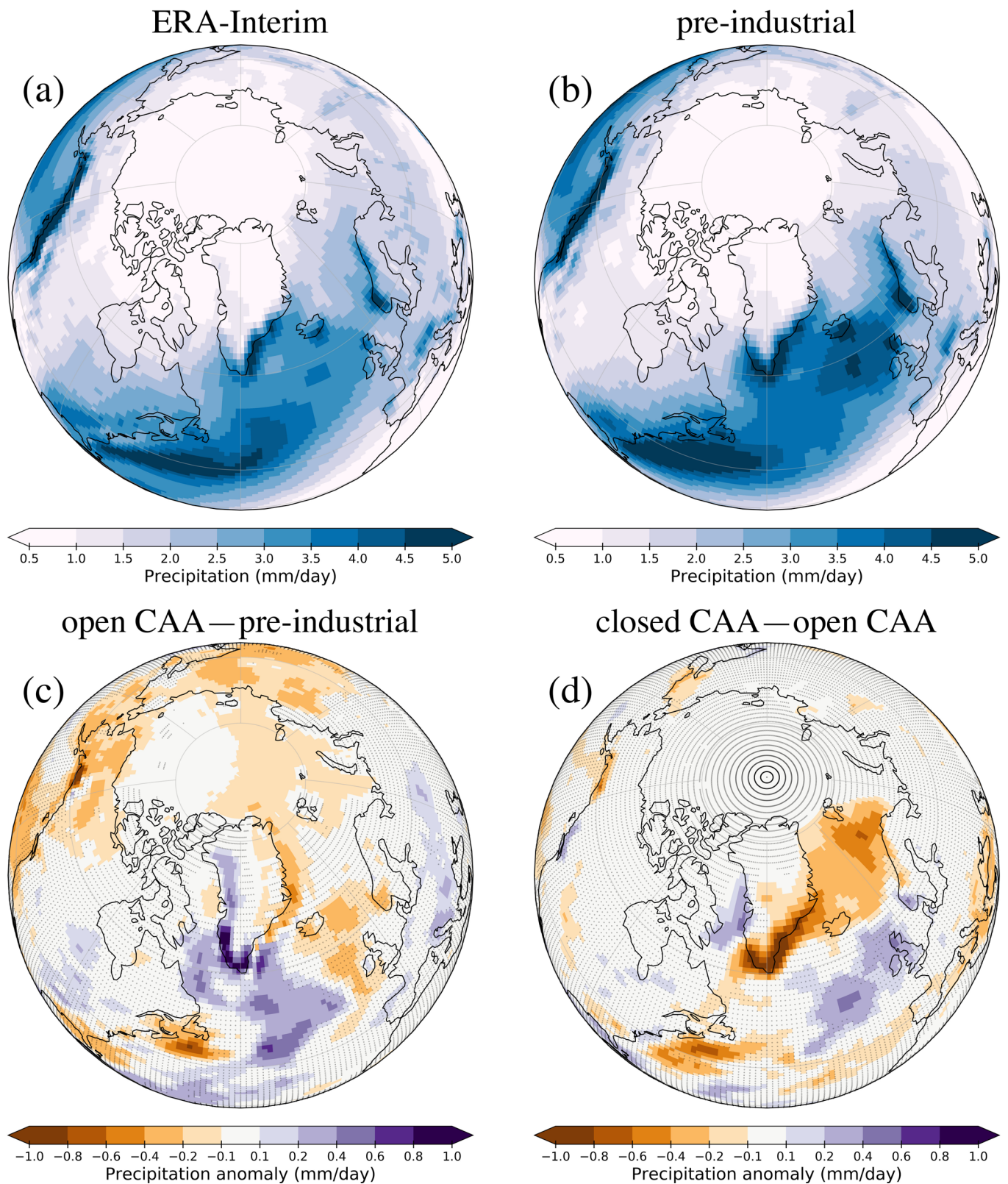
Mapping software: Cartopy with Natural Earth shapefiles.



Extended Data Fig. 7 | Comparison of June-August (JJA) mean surface temperature. from (a) ERA-Interim reanalysis product⁶¹ (averaged over years 1979–2014) and (b) the pre-industrial simulation; surface temperature anomalies in the 116 ka simulations with (c) open and (d) closed CAA gateways. Arrows in panels (c) and (d) indicate 850 hPa horizontal wind vectors (full zonal and meridional wind components in open CAA and closed CAA, respectively). Red arrows between 55°–80°N & 15°W–50°E roughly indicate the region where cool temperatures in the Nordic Seas are advected into Scandinavia, yielding favorable conditions for glacial inception in the highland regions of Norway and Sweden in the simulation with closed CAA gateways (panel d). Mapping software: Cartopy with Natural Earth shapefiles.



Extended Data Fig. 8 | Timeseries of annually integrated temperature in the Scandinavian Mountains above 1000 m elevation. Temperature data was averaged over all grid cells where the topography in the Scandinavian mountain range is over 1000 m elevation (region: 58°–78°N; 13°W–20°E) on the 4-km ice-sheet model grid (see Methods). Light colours indicate annually resolved temperature, and heavy lines show 10-year rolling averages to highlight the long-term temperature trend. The dashed and dotted vertical lines (at model years 725 and 739, respectively) indicate inception at the southern and the northern locations in the simulation with closed CAA gateways (see Fig. 4). Note that the pre-industrial control simulation was not run with the extended ice-sheet model grid, hence we do not have access to downscaled temperature data from that simulation. Moreover, the ice-sheet model only outputs annual mean temperature, which precludes a seasonal decomposition.



Extended Data Fig. 9 | Comparison of annual mean precipitation. (a) Full precipitation (liquid+solid) from the ERA-Interim reanalysis product⁶¹ (averaged over years 1979–2014) and (b) the pre-industrial simulation; precipitation anomalies in the 116 ka simulation with (c) open CAA and (d) closed CAA ocean gateways, respectively. Stippling in panels (c) and (d) indicates differences that are not significant at the 95% level. Mapping software: Cartopy with Natural Earth shapefiles.